Nano Research

Open Access

Research Article

Sulfur vacancy and heterointerface synergistically regulated $VS_4@Bi_2S_3$ for high-capacity and long-life magnesium-ion batteries

Jingtian Zeng[1,3], Shaobo Xia[1], Pengyun Xie[1], Xuan Xie[1], Hui Peng[1]✉, Lei Zhu[2]✉, Imran Shakir[4]✉, Guofu Ma[1], and Yuxi Xu[3]✉

[1] *Key Laboratory of Eco-functional Polymer Materials of the Ministry of Education, Key Laboratory of Polymer Materials of Gansu Province, College of Chemistry and Chemical Engineering, Northwest Normal University, Lanzhou 730070, China*
[2] *School of Chemistry and Materials Science, Hubei Engineering Research Center for Key Technologies in Modern Paper and Sanitary Products Manufacturing, Hubei Engineering University, Xiaogan 432000, China*
[3] *School of Engineering, Westlake University, Hangzhou 310024, China*
[4] *Department of Physics, Faculty of Science, Islamic University of Madinah, Madinah 42351, Saudi Arabia*

Cite this article: *Nano Research*, **2026**, *19*, 94908461. https://doi.org/10.26599/NR.2026.94908461

ABSTRACT: Rechargeable magnesium-ion batteries (RMBs) are considered promising energy storage devices due to their high energy density, low-cost, and reliable safety. However, their development is still constrained by problems such as sluggish Mg^{2+} diffusion kinetics and poor structural stability. Herein, an urchin-like $VS_4@Bi_2S_3$ heterostructure cathode with moderate sulfur vacancy concentration and well-defined heterointerfaces has been successfully constructed through *in-situ* growing Bi_2S_3 nanorods on VS_4 microspheres via rapid (25 min) microwave-assisted solvothermal method. The appropriate sulfur vacancies provide abundant active sites while mitigating structural degradation caused by excessive defects. Besides, the material forms a Type-II heterojunction via V-S-Bi interfacial chemical bridging, inducing a built-in electric field that significantly enhances electron transport, facilitates Mg^{2+} adsorption (−1.90 eV) and diffusion (energy barrier of 0.47 eV), and buffers volume changes during cycling. Electrochemical evaluations demonstrate that the optimized $VS_4@Bi_2S_3$ electrode delivers an initial discharge capacity of 1407.69 mAh·g^{-1} and stabilized at about 353.50 mAh·g^{-1} at 0.05 A·g^{-1}, which is significantly higher than that of VS_4 (227.31 mAh·g^{-1}) and Bi_2S_3 (152.29 mAh·g^{-1}). A combination of *ex-situ*/*in-situ* characterization and theoretical simulations reveals the synergistic magnesium storage mechanism involving intercalation and nanoconfined conversion reactions, along with interfacial dynamic stabilization. This work offers new insights into rational material design and mechanistic understanding for developing high energy density and long-life RMBs.

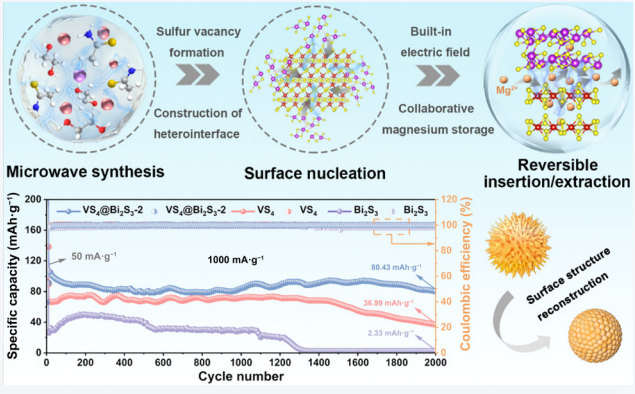

KEYWORDS: heterostructure, sulfur vacancy, interface engineering, cathode material, magnesium-ion battery

1 Introduction

Driven by the global goal of carbon neutrality, the development and utilization of renewable energy sources, such as solar, wind, and geothermal power have gained worldwide consensus. However, the inherent intermittency, geographical constraints, and instability of renewables necessitate the support of large-scale energy storage technologies to facilitate a reliable energy transition [1–3]. In this context, electrochemical energy storage has emerged as a key enabler, with metal-ion batteries playing a central role. Among them, lithium-ion batteries (LIBs) have long dominated markets for portable electronics and electric vehicles. However, their sustainable application in grid-scale energy storage is increasingly challenged by the scarcity and uneven distribution of lithium resources, coupled with rising costs and supply chain vulnerabilities. To diversify energy storage technologies, research into alternative metal-ion batteries has intensified [4, 5]. Sodium-ion batteries (SIBs), though cost-effective due to abundant sodium resources, still suffer from

Received: December 3, 2025; **Revised:** January 14, 2026
Accepted: January 19, 2026

✉Address correspondence to Hui Peng, penghui@nwnu.edu.cn; Lei Zhu, Lei.zhu@hbeu.edu.cn; Imran Shakir, mshakir@iu.edu.sa; Yuxi Xu, xuyuxi@westlake.edu.cn

limited energy density [6, 7]. In comparison, rechargeable magnesium-ion batteries (RMBs) present a compelling combination of advantages. For example, magnesium (Mg) is not only earth-abundant and low-cost, but also offers a high theoretical volumetric capacity of 3833 mAh·cm^{-3}, which is significantly surpassing that of lithium and sodium [8–10]. More importantly, magnesium exhibits minimal to dendrite formation during plating/stripping processes, which substantially improves safety [11–13].

Despite the promising potential of RMBs, their commercialization still faces the major challenge of developing high-performance cathode materials (such as high capacity, fast kinetics, highly reversible Mg^{2+} insertion/extraction and structural stability) [14–16]. There is usually a strong Coulombic interaction between the double-charged Mg^{2+} ions and the host lattice framework, which leads to sluggish solid-state diffusion kinetics and consequently significant polarization, limited specific capacity, and poor rate performance. Thus, cathode materials represent a critical bottleneck restricting the overall electrochemical performance of RMBs [17, 18]. Extensive research has been devoted to exploring various cathode systems, including Chevrel phases, layered oxides, polyanionic compounds, and conversion-type materials [19, 20]. Among them, transition metal sulfides (TMS) stand out due to their unique structural advantages. Compared to their corresponding oxides, TMS possess a more flexible anion lattice, and the higher polarizability of S^{2-} ions helps screen the strong Coulombic attraction between Mg^{2+} and the host framework, thereby reducing the diffusion energy barrier. Moreover, TMS materials often enable multi-electron transfer redox reactions, which contribute to higher specific capacity [21–23].

To further enhance the magnesium storage capacity of TMS, researchers have developed a series of effective material modification strategies, including defect engineering and the construction of heterostructures [24–26]. For example, Chen et al. employed an interlayer cationic defect engineering strategy to incorporate Mg^{2+} into the lamellar framework of sodium vanadate, forming a defect-rich d-MgNVO cathode [24]. The intercalated Mg^{2+} defects serve as structural pillars and electronic modulators, confining the diffusion pathways of Mg^{2+} along a favorable direction and inducing a semiconductor-to-conductor transition via 3d orbital splitting. This electronic restructuring lowers the migration energy barrier and enhances both ionic and electronic conductivities. As a result, the d-MgNVO cathode achieves superior magnesium storage performance, enabling a high reversible capacity of 33.2 mAh·g^{-1} after 5000 cycles in a full cell. Jiang et al. developed a microwave-induced defect engineering strategy to construct a synergistic defect structure in VS_4 featuring abundant sulfur vacancies and V^{3+} self-doping [25]. The lattice charge redistribution induced by sulfur vacancies, combined with valence state modulation between V^{3+}/V^{4+}, directly regulates the electronic structure and ion transport pathways of VS_4. This effectively suppresses irreversible structural distortion during cycling, enabling a retained capacity of 48.63 mAh·g^{-1} after 800 cycles at 1.0 A·g^{-1}. Zhang et al. constructed a V_2C@VS_4 heterostructure through a one-step hydrothermal interfacial coupling strategy [26]. The V–S covalent bonds formed between V_2C MXene and VS_4 induce electron transfer from V_2C to VS_4, directly regulating the electronic structure of the interface and facilitating the formation of a built-in electric field. This significantly enhances the interfacial charge transfer kinetics and Mg^{2+} diffusion rate, while effectively suppressing the structural collapse of V_2C layers and the agglomeration of VS_4 during cycling. As a result, the V_2C@VS_4 heterostructure exhibits an outstanding long-cycle stability. In this manner, a cathode material ingeniously designed to combine a defect engineering with a heterogeneous interface construction strategy holds promise for overcoming the challenges.

VS_4 is known for its 1D linear chain structure, where the wide interchain spacing and weak van der Waals interactions facilitate Mg^{2+} intercalation. However, VS_4 exhibits poor intrinsic electronic conductivity and is prone to structural degradation and severe polarization during cycling, leading to rapid capacity fading and unsatisfactory rate performance [27, 28]. Bi_2S_3 possesses a layered semiconductor structure that also favors ion insertion/extraction. In RMBs, Bi_2S_3 undergoes a multi-electron conversion-alloying reaction, offering a substantial capacity basis for magnesium storage. Moreover, its use as a cathode effectively mitigates magnesium anode passivation, thereby promoting reversible Mg^{2+} plating/stripping and improving overall electrochemical reversibility [29]. Nonetheless, Bi_2S_3 also suffers from low conductivity and structural stacking collapse during repeated charge–discharge cycles, resulting in poor long-term stability [30]. To address these limitations, we designed a VS_4@Bi_2S_3 heterostructure in this work, which consists of Bi_2S_3 nanorods epitaxially grown from a spherical VS_4 cores. In particularly, sulfur vacancies were introduced using a microwave-assisted solvothermal method, effectively integrating defect engineering with heterointerface construction. An optimized VS_4@Bi_2S_3 heterostructure (VS_4@Bi_2S_3-2) with moderate sulfur vacancies and a well-defined heterointerface was obtained by adjusting the molar ratio of vanadium to bismuth sources. The controlled vacancy concentration provides abundant active sites without compromising structural integrity, while the heterointerface enhances charge transfer and accommodates volume variation during cycling. As a result, the VS_4@Bi_2S_3-2 electrode delivers a high initial discharge capacity of 1407.69 mAh·g^{-1} at 0.05 A·g^{-1}, along with remarkable rate capability and extended cycling durability. The capacity retention rate is approximately 91.4% after 2000 cycles at 1 A·g^{-1}. This work establishes a new paradigm for coupling defect and heterointerface engineering, highlighting the importance of designing cathodes with high electronic and ionic conductivity alongside high structural stability for practical RMBs.

2 Results and discussion

Figure 1(a) illustrates the synthesis of VS_4@Bi_2S_3, in which abundant VS_4 nuclei initially form throughout the solution. To minimize surface energy, these nuclei evolve into spherical nanoparticles, serving as high-surface-area heterogeneous substrates for the subsequent deposition of Bi_2S_3. Microwave heating enables rapid and uniform temperature rise, promoting concurrent nucleation and growth of both VS_4 and Bi_2S_3 while suppressing their independent precipitation. The rapid thermal effect further enhances ion exchange, disrupting the lattice integrity of VS_4 and inducing a high density of sulfur vacancies [31]. The semiconducting nature of VS_4 and Bi_2S_3 originates from their confined valence and conduction bands [32]. During heterojunction formation, strong orbital hybridization occurs at the interface: V 3d and Bi 6p orbitals hybridize with S 3p orbitals, forming robust V-S-Bi chemical bridges that facilitate heterointerface formation. Figures 1(b) and 1(c) present scanning electron microscopy (SEM) images of the VS_4@Bi_2S_3

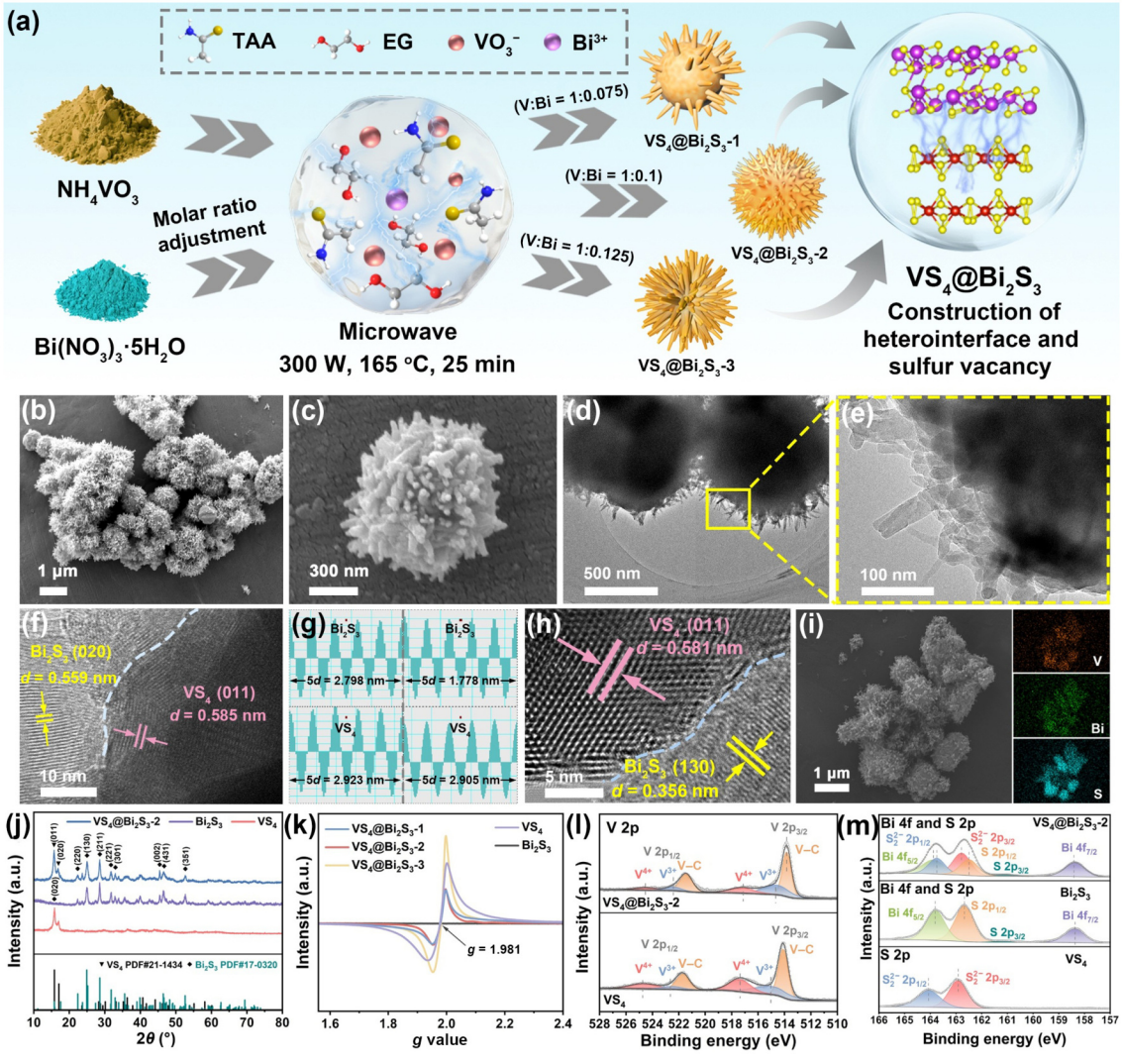

Figure 1 (a) Schematic illustration of the synthesis of $VS_4@Bi_2S_3$. (b) and (c) SEM images, (d) and (e) TEM images, and (f)–(h) HRTEM images of $VS_4@Bi_2S_3$-2. (i) SEM image and corresponding EDS map of $VS_4@Bi_2S_3$-2. (j) XRD patterns of VS_4, Bi_2S_3, and $VS_4@Bi_2S_3$-2. (k) EPR patterns of VS_4, Bi_2S_3 and $VS_4@Bi_2S_3$. (l) High-resolution XPS spectra of V 2p for VS_4 and $VS_4@Bi_2S_3$-2. (m) High-resolution XPS spectra of Bi 4f and S 2p for VS_4, Bi_2S_3, and $VS_4@Bi_2S_3$-2.

heterostructure. For comparison, VS_4, Bi_2S_3, and $VS_4@Bi_2S_3$ with varying bismuth precursor ratios were synthesized under similar conditions. The $VS_4@Bi_2S_3$ samples prepared with vanadium to bismuth sources at molar ratios of 1:0.075, 1:0.1, and 1:0.125 are denoted as $VS_4@Bi_2S_3$-1, $VS_4@Bi_2S_3$-2, and $VS_4@Bi_2S_3$-3, respectively. SEM images reveal that VS_4 appears as uniform microspheres, while bare Bi_2S_3 appears as nanoparticles (Fig. S1 in the Electronic Supplementary Material (ESM)). In contrast, an urchin-like $VS_4@Bi_2S_3$ architecture is observed in the nanocomposite (Fig. S2 in the ESM), indicating that Bi_2S_3 grows into a spinous morphology via epitaxial growth on the VS_4 microsphere core, and that they can form a robust heterostructure. Furthermore, with increase of bismuth content, the heterostructure evolves from incomplete short-nanorod coverage ($VS_4@Bi_2S_3$-1) to a dense long-spines epitaxial layer ($VS_4@Bi_2S_3$-3), while the $VS_4@Bi_2S_3$-2 exhibits uniform urchin-like morphology with appropriate and vertical nanorods features. Transmission electron microscope (TEM) images further confirm the nanorods-on-microsphere nanocomposite architecture (Figs. 1(d) and 1(e)). High-resolution TEM (HRTEM) reveals lattice fringes of 0.581, 0.559, and 0.356 nm in $VS_4@Bi_2S_3$, corresponding to the (011) crystal plane of VS_4 and the (020) and (130) crystal planes of Bi_2S_3 (Figs. 1(f)–1(h)), respectively. Clear grain boundaries between spines and microsphere domains confirm successful heterojunction formation. Selected-area energy-dispersive X-ray spectroscopy (EDS) patterns in Fig. 1(i) and Figs. S3 and S4 in the ESM reveal the uniform distribution of V, Bi, and S elements within the respective samples. X-ray diffraction (XRD) confirms the coexistence of both phases, with Bi_2S_3 peak intensities increasing with bismuth content (Fig. 1(j) and Fig. S5 in the ESM). Notably, the enhanced (020) diffraction peak of Bi_2S_3 suggests lattice matching with the (011) crystal plane of VS_4, consistent with HRTEM observations [33, 34]. The $VS_4@Bi_2S_3$ possesses a specific surface area of 57.19 $m^2·g^{-1}$, higher than those of VS_4 (44.39 $m^2·g^{-1}$) and Bi_2S_3 (48.73 $m^2·g^{-1}$) (Fig. S6 in the ESM). The increased surface area promotes active site accessibility and electrolyte wettability, thereby enhancing magnesium storage. Moreover, the pore size distribution curves reveal that the $VS_4@Bi_2S_3$ heterostructure retains rich micropores (< 2 nm) and mesopores (2–30 nm), offering efficient pathways for Mg^{2+} transport.

As shown in Fig. 1(k), in the electron paramagnetic resonance (EPR) test at low temperature (100 K), VS_4 and the series $VS_4@Bi_2S_3$ heterostructure exhibited a characteristic resonance signal with a *g*-

value of 1.981, which can be attributed to the paramagnetic centers formed by sulfur vacancies capturing unpaired electrons [25, 35]. It can be observed that the sulfur vacancy concentration does not change monotonically with increasing bismuth source content, since the intensity of the EPR signal reflects the relative concentration of sulfur vacancies. This phenomenon reveals the competition between the two effects of "interface strain induced defects" and "interface bonding repair defects" in the formation process of heterojunctions [36, 37]. Bi_2S_3 forms moderate epitaxial coverage on the VS_4 surface, where interfacial bonding effectively repairs intrinsic sulfur vacancies on the VS_4 surface, resulting in lower EPR signal intensities for VS_4@Bi_2S_3-1 and VS_4@Bi_2S_3-2 compared to pure VS_4. Conversely, introducing more bismuth sources induces significant interfacial lattice mismatch and strain. To release strain energy, the system tends to induce new sulfur vacancies near the VS_4 interface, resulting in higher sulfur vacancy concentrations in VS_4@Bi_2S_3-3 compared to pure VS_4 [38, 39]. To further analyze the electron flow and atomic chemical states within the heterostructure, X-ray photoelectron spectroscopy (XPS) measurements were performed on VS_4, Bi_2S_3, and VS_4@Bi_2S_3 samples. The survey spectra reveal characteristic elemental peaks corresponding to VS_4 and Bi_2S_3 within VS_4@Bi_2S_3-2 (Fig. S7 in the ESM). Figures 1(l) and 1(m) display the high-resolution XPS spectra of V 2p, Bi 4f, and S 2p for VS_4 and Bi_2S_3, as well as the VS_4@Bi_2S_3 nanocomposite. Compared to VS_4 and Bi_2S_3, the V 2p and S 2p peaks in the VS_4@Bi_2S_3-2 nanocomposite shift toward lower binding energies, while the Bi 4f peak shifts toward higher binding energies. This arises from Fermi level alignment between the two semiconductors, resulting in reduced electron density around Bi atoms and increased electron density around V atoms. This indicates electron transfer from Bi_2S_3 to VS_4, confirming the formation of a built-in electric field at the VS_4@Bi_2S_3 heterointerface [40].

Density functional theory (DFT) calculations were employed to predict the magnesium storage capacity of VS_4, Bi_2S_3, and the VS_4@Bi_2S_3 nanocomposite. This evaluation encompassed charge transfer, electronic state distribution, and the adsorption/diffusion kinetics of magnesium ions. The computational models for VS_4, Bi_2S_3, and the VS_4@Bi_2S_3 nanocomposite are present in Figs. S8–S10 in the ESM. As clearly shown by the differential charge calculations and 2D cross-sectional diagrams of VS_4@Bi_2S_3 in Figs. 2(a)–2(c), the electron density decreases around Bi_2S_3 at the heterointerface while increasing near VS_4. This further confirms that electrons flow from the bulk Bi_2S_3 toward VS_4 at the heterointerface. Notably, the electron cloud within VS_4 undergoes localized polarization, enhancing the stability of the heterointerface bonding. Additionally, adsorption energy calculations were performed for the Mg^{2+} structures on optimized VS_4, Bi_2S_3, and VS_4@Bi_2S_3 (Fig. 2(d)). The VS_4@Bi_2S_3 heterostructure exhibits a lower adsorption energy (−1.90 eV) than VS_4 (−0.59 eV) and Bi_2S_3 (−1.06 eV), indicating that the heterostructure enhances Mg^{2+} capture capacity to facilitate subsequent Mg^{2+} insertion. In addition, density of states (DOS) calculations was performed to reveal the electronic structures in the three configurations (Figs. 2(e)–2(h)). According to the calculations, the bandgap of VS_4, Bi_2S_3 and VS_4@Bi_2S_3 is 0.643, 1.488, and 0.310 eV, respectively. The total DOS in Fig. 2(e) clearly demonstrates that the VS_4, Bi_2S_3, and the VS_4@Bi_2S_3 nanocomposite all exhibit semiconductor properties. Strong interfacial interactions significantly reduce the overall bandgap of the nanocomposite material, enhancing its intrinsic conductivity [41]. More importantly, the reduced density of states peak near the Fermi level reveals electronic state restructuring caused by interfacial orbital hybridization. This provides an ideal pathway for the effective spatial separation of electron–hole pairs, theoretically predicting superior electrochemical performance, which is in line with our expectations. The partial density of states (PDOS) in Figs. 2(f)–2(h) further reveals strong intramolecular orbital hybridization within both VS_4 and Bi_2S_3, as well as within the VS_4@Bi_2S_3 nanocomposite, while the heterointerface exhibits high stability. Notably, in the valence band region, the heterostructure utilizes S p orbitals as a bridge to mediate hybridization between V d and Bi p orbitals. In the conduction band region, V d orbitals become dominant, incorporating S p and Bi p orbitals into their extended electronic states. This coexistence of band-dominated partitioning and cross-boundary orbital hybridization constitutes a typical Type-II heterojunction electronic structure, providing an ideal electronic pathway for achieving efficient interfacial charge separation and rapid electron transport [42]. To further investigate the kinetic evolution of Mg^{2+} diffusion, the corresponding diffusion energy barriers were simultaneously calculated based on the diffusion pathways of Mg^{2+} along the surfaces of VS_4 and Bi_2S_3, as well as at the VS_4@Bi_2S_3 heterointerface (Figs. 2(i)–2(k)). As shown in Fig. 2(l), the diffusion energy barrier for VS_4@Bi_2S_3 (0.47 eV) is significantly lower than that for pristine VS_4 (0.84 eV) and Bi_2S_3 (0.67 eV), indicating superior Mg^{2+} diffusion kinetics at the VS_4@Bi_2S_3 heterointerface. The formation of an intrinsic electric field provides an electrostatic driving force that substantially reduces the barrier to Mg^{2+} diffusion.

To ensure the electrochemical performance evaluation in this study is based on a stable battery system, we systematically characterized the selected electrolyte and the magnesium metal interface. Linear sweep voltammetry (LSV) tests (Fig. S11 in the ESM) indicate that the reduction stability limit of this electrolyte is approximately 0.1 V vs. Mg^{2+}/Mg, while its oxidation stability limit exceeds 2.0 V, providing a foundation for the operational voltage window of 0.1–1.8 V. Mg||Mg symmetric battery testing serves as an effective method for assessing interface stability. The battery exhibits a stable, low overpotential and can cycle steadily for over 200 h without signs of short-circuiting (Fig. S12 in the ESM), demonstrating good reversibility of Mg plating/stripping and favorable interfacial stability. In addition, our analysis of the cycled copper current collector and stainless-steel hardware (Fig. S13 in the ESM) demonstrates that both the copper foil and the stainless-steel components remain macroscopically intact without significant signs of dissolution or corrosion. The results indicate that although the potential decreases after cycling within the 0.1–1.8 V, the corrosiveness of the selected electrolyte system to the battery hardware is negligible.

To evaluate the impact of the voltage window and electrolyte decomposition on capacity, we compared the electrochemical performance at different lower cut-off voltages (Fig. S14 in the ESM). When the lower cut-off voltage was increased from 0.1 to 0.2 V, the initial discharge capacity decreased from 1407.7 to 1044.5 mAh·g^{-1}. When the cut-off was further raised to 0.4 V, the initial discharge capacity dropped to 779.8 mAh·g^{-1}. This result confirms that a substantial portion of the capacity (approximately 363.2 mAh·g^{-1}) originates from irreversible processes occurring below 0.2 V. However, the initial Coulombic efficiency (ICE) did not improve systematically with the increase in cut-off voltage. At 0.4 V, the ICE was 47.4%, slightly lower than the 49.3% at 0.1 V.

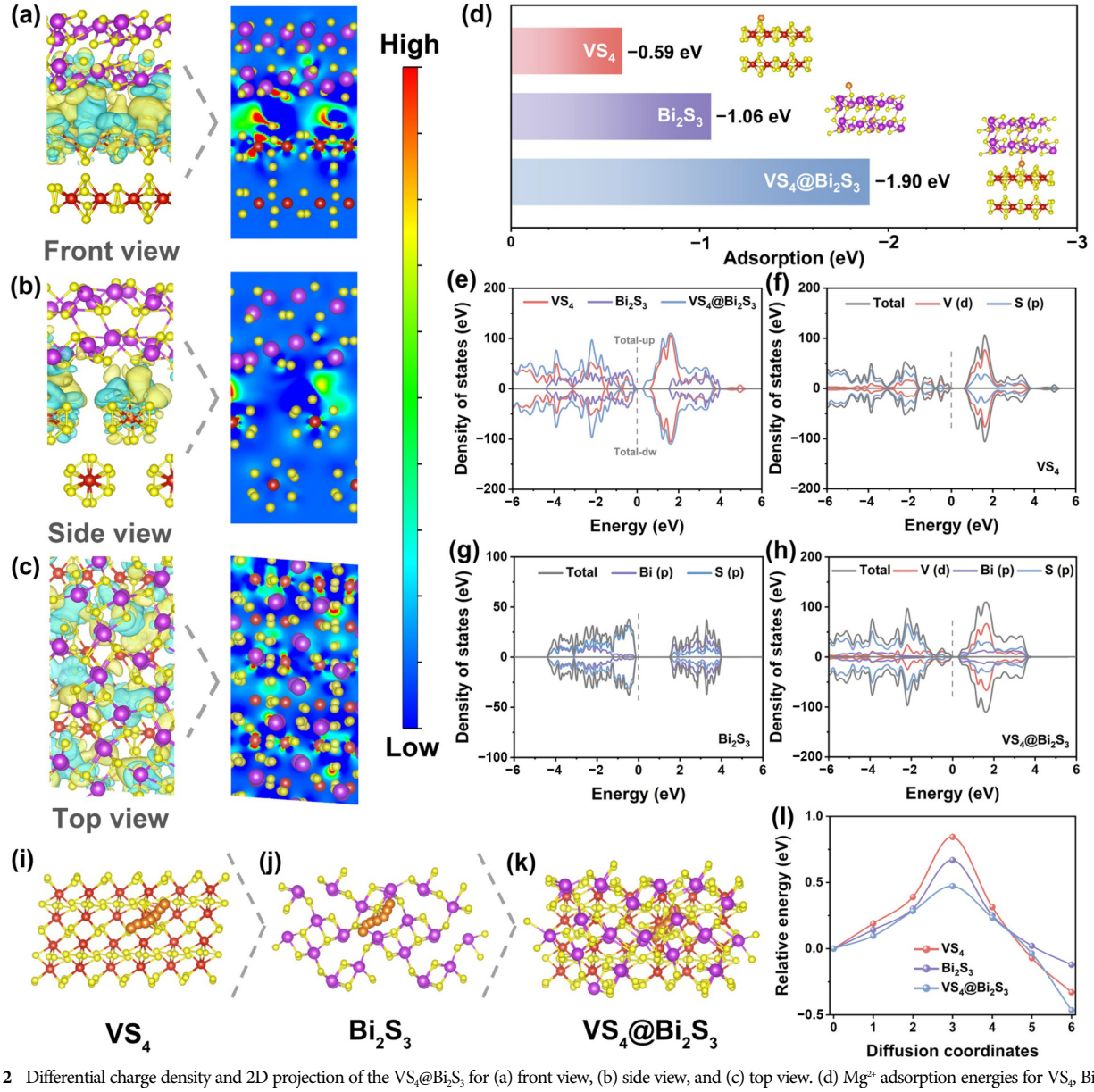

Figure 2 Differential charge density and 2D projection of the $VS_4@Bi_2S_3$ for (a) front view, (b) side view, and (c) top view. (d) Mg^{2+} adsorption energies for VS_4, Bi_2S_3, and $VS_4@Bi_2S_3$. (e) DOS and (f)–(h) PDOS for VS_4, Bi_2S_3, and $VS_4@Bi_2S_3$. (i)–(k) Schematic migration pathways of Mg^{2+} in VS_4, Bi_2S_3, and $VS_4@Bi_2S_3$. (l) Diffusion energy barriers for Mg^{2+} in VS_4, Bi_2S_3, and $VS_4@Bi_2S_3$.

This may be due to slower kinetics of magnesium intercalation at higher cut-off voltages, which allows charge to be more readily consumed by persistent interfacial side reactions. Furthermore, to directly quantify the contribution from electrolyte decomposition, a pure carbon electrode was tested within a voltage range of 0.1–1.8 V (Fig. S15 in the ESM). The results show that the capacity contributed solely by electrolyte decomposition is about 41.6 $mAh \cdot g^{-1}$. This value is significantly lower than the total observed irreversible capacity, indicating that the major irreversible consumption is not due to bulk electrolyte decomposition but is closely related to more complex interfacial reactions occurring on the surface of $VS_4@Bi_2S_3$ heterojunction material with high surface area. These reactions may include the irreversible reduction of electrolyte at defects and active sites, as well as the formation of cathode/electrolyte or solid electrolyte interphase (CEI/SEI) layers accompanying Mg^{2+} intercalation/conversion reactions. Thus, the voltage window of 0.1–1.8 V was selected for this study to fully exploit the intrinsic advantages of this heterojunction material in terms of reversible capacity and cycling life, while ensuring that the electrolyte does not undergo significant decomposition.

Based on the superior structural characteristics of $VS_4@Bi_2S_3$ and supported by DFT theoretical calculations, it was assembled into a half-battery with Mg foil as the counter electrode to evaluate its Mg^{2+} storage performance. Figures 3(a)–3(c) show the initial five-cycle cyclic voltammetry (CV) curves of the VS_4, Bi_2S_3, and $VS_4@Bi_2S_3$-2 electrodes at 0.1 $mV \cdot s^{-1}$, respectively. The results indicate that the redox process of $VS_4@Bi_2S_3$-2 encompasses characteristic peaks from both VS_4 and Bi_2S_3. As cycling progressed, polarization decreased for VS_4 while increasing for Bi_2S_3, indicating gradual activation of VS_4 and potential agglomeration of Bi_2S_3 nanoparticles [43]. Of significance is that the nanocomposite structure exhibits the same activation phenomenon as VS_4 while

suppressing the tendency for increased polarization in Bi_2S_3. This indicates that the support and interfacial coupling effects of VS_4 stabilize the Bi_2S_3 structure, buffer volume changes, and mitigate Bi_2S_3 agglomeration during charging and discharging. The synergistic contribution of both components enhances the reversibility of the reaction. Figure 3(d) shows the short-cycle performance of VS_4, Bi_2S_3, and VS_4@Bi_2S_3 at a current density of 50 mA·g^{-1}. The initial discharge capacities of VS_4, Bi_2S_3 and VS_4@Bi_2S_3 are 989.46, 1175.23 and 1407.69 mAh·g^{-1}, and their ICE are 41.8%, 14.8% and 49.3%, respectively. The increased specific surface area of the nanocomposite leads to lower ICE due to the formation of the solid electrolyte interphase (SEI) film. However, it rapidly recovers and stabilizes at 100% after 10 cycles. The high discharge capacity of the VS_4@Bi_2S_3 nanocomposite confirms that the heterojunction enhances ion diffusion, while sulfur vacancies promote the full utilization of active sites, effectively boosting magnesium storage capacity.

The galvanostatic charge–discharge (GCD) curves for VS_4, Bi_2S_3 and VS_4@Bi_2S_3-2 are shown in Fig. 3(e) and Fig. S16 in the ESM. During the first five cycles, the VS_4@Bi_2S_3 nanocomposite clearly exhibits characteristic potential plateaus corresponding to the magnesium ion insertion into VS_4 and Bi_2S_3, respectively, confirming the synergistic contribution of both components. After 50 cycles, the discharge specific capacity of VS_4@Bi_2S_3 nanocomposite stable at 389.42 mAh·g^{-1}, which is significantly higher than that of VS_4 (240.28 mAh·g^{-1}) and Bi_2S_3 (93.66 mAh·g^{-1}). Additionally, the discharge plateau of the VS_4@Bi_2S_3 nanocomposite, especially bare Bi_2S_3, shortened from 0.2 to 0.1 V

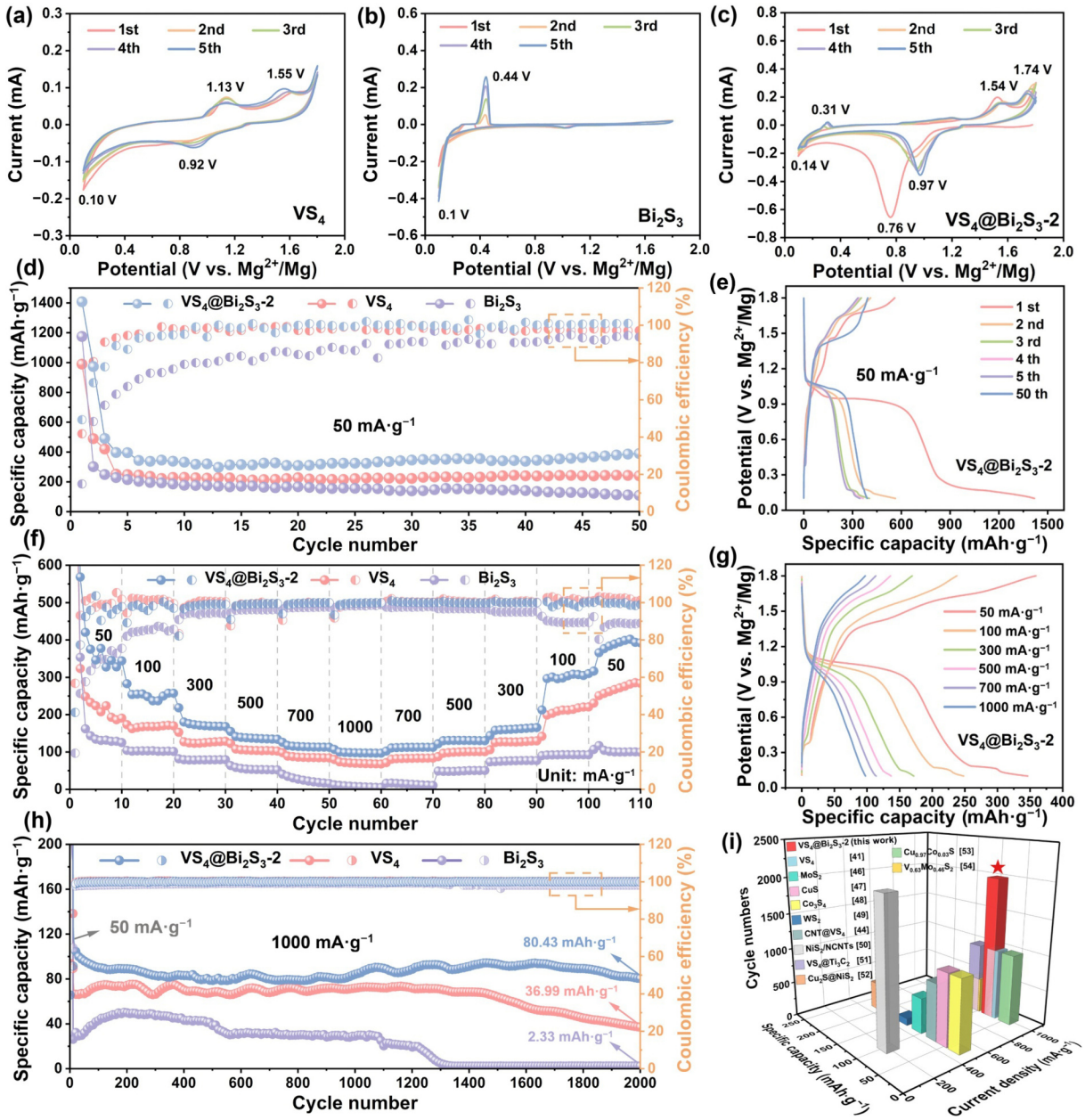

Figure 3 CV curves of (a) VS_4, (b) Bi_2S_3, and (c) VS_4@Bi_2S_3-2. (d) Short-cycle performance of VS_4, Bi_2S_3, and VS_4@Bi_2S_3-2. (e) GCD curve of VS_4@Bi_2S_3-2 at 50 mA·g^{-1}. (f) Rate performance of VS_4, Bi_2S_3, and VS_4@Bi_2S_3-2. (g) GCD curves of VS_4@Bi_2S_3-2 at current densities from 50 to 1000 mA·g^{-1}. (h) Long-term cycling performance of VS_4, Bi_2S_3, and VS_4@Bi_2S_3-2. (i) Performance comparison of VS_4@Bi_2S_3-2 with previously reported sulfide-based RMBs cathodes [41, 44, 46–54].

after multiple cycles, which is attributed to the structural collapse and reconstruction of the epitaxial Bi_2S_3 due to volume expansion. Figure 3(f) compares the rate performance of VS_4, Bi_2S_3, and VS_4@Bi_2S_3-2 at current densities of 0.05, 0.1, 0.3, 0.5, 0.7, and 1.0 A·g^{-1}. At corresponding current densities, the discharge specific capacities of the VS_4@Bi_2S_3 nanocomposite are 374.99, 248.17, 171.58, 136.99, 113.92, and 97.66 mAh·g^{-1}, respectively. When the current density was restored to 0.05 A·g^{-1}, it still maintained a reversible specific capacity higher than that of the initial cycle (392.24 mAh·g^{-1}), indicating that VS_4@Bi_2S_3 exhibits excellent reversibility. This result can be attributed to the stable heterointerface that alleviates the stress during charging and discharging and maintains good electronic conduction and ion transport. Furthermore, the GCD curves of the VS_4@Bi_2S_3 nanocomposite at different current densities further demonstrate its superior rate performance compared to bare VS_4 and Bi_2S_3 (Fig. 3(g) and Fig. S17 in the ESM). To further investigate the impact of heterointerface construction on electrochemical performance, long-term cycling performance was evaluated (Fig. 3(h)). Specifically, it was first cycled 10 cycles at 0.05 A·g^{-1} to form a stable SEI film and activate active sites, and then the current density was increased to 1.0 A·g^{-1} for subsequent cycling tests. One can clearly see that VS_4@Bi_2S_3-2 exhibits higher discharge specific capacity and superior cycling stability than bare VS_4 and bare Bi_2S_3. After 2000 cycles, the capacity of VS_4@Bi_2S_3-2 remained at 80.43 mAh·g^{-1} with capacity retention rate of 91.4%, significantly higher than that of pure VS_4 (36.99 mAh·g^{-1}, 50.9%) and pure Bi_2S_3 (2.33 mAh·g^{-1}, 7.7%). Furthermore, we conducted reproducibility tests on multiple batteries of VS_4@Bi_2S_3-2. Figure S18 in the ESM displays the cycling performance and the corresponding average Coulombic efficiency of three independent batteries at 1.0 A·g^{-1}. The results indicate that the capacity fluctuations observed during long-term cycling may originate from the local, dynamic reconstruction of the active material. The heterojunction interfaces and the moderate sulfur vacancies effectively buffer the volume stress, limit the extent of irreversible phase transformations and side reactions, and confine the unstable conversion reactions within highly reversible nanoscale domains [44]. We also compared the electrochemical processes and performance of VS_4@Bi_2S_3 with different bismuth source contents (Fig. S19 in the ESM). Although VS_4@Bi_2S_3-1, VS_4@Bi_2S_3-2, and VS_4@Bi_2S_3-3 exhibited similar electrochemical processes and comparable total capacities, their reaction pathway distribution and cycling stability showed significant differences. With increasing bismuth content, the discharge plateau of VS_4@Bi_2S_3 is prolonged in the range of 0.2 to 0.1 V, while the plateau from 1.2 to 0.8 V shortens to some extent. This indicates reaction pathway optimization and active site competition regulated by the heterointerface throughout the discharge process. Figure S20 in the ESM compares the short-cycle performance, rate performance, and long-cycle performance of various VS_4@Bi_2S_3 electrodes, which results indicate that VS_4@Bi_2S_3-2 exhibits the most stable cycling performance. For VS_4@Bi_2S_3-1, insufficient bismuth supply resulted in deficient coverage of the Bi_2S_3 nanorods on VS_4 microsphere. Although this discontinuous heterojunction promoted ion migration to some extent, it tended to become a stress concentration point during cycling, accelerating the overall structural degradation. For VS_4@Bi_2S_3-3, a higher bismuth source induces the generation of high-concentration sulfur vacancies. While these vacancies provide abundant active sites, they also severely compromise the integrity of the crystal structure, causing the material to suddenly collapse due to accumulated structural damage during long-term cycling, manifesting as battery overcharge failure [45]. In contrast, the moderate sulfur vacancy concentration in VS_4@Bi_2S_3-2 provides essential active sites while avoiding the instability caused by uneven coating layers and high defect concentrations, thus making it a preferred sample for detailed study. Furthermore, among most existing sulfide-based cathode materials for RMBs, VS_4@Bi_2S_3-2 exhibits superior electrochemical performance (Fig. 3(i) and Table S1 in the ESM). In summary, this study successfully combined defect engineering with heterointerface engineering to precisely design VS_4@Bi_2S_3 nanocomposites with structural advantages and enhanced electrochemical performance through composition control. This approach provides novel insights and effective strategies for designing RMBs cathode materials that simultaneously achieve high capacity and long cycle life.

To further analyze the electrode reaction kinetics and evolution of interfacial electrochemical behavior in the VS_4@Bi_2S_3 heterostructure, the magnesium storage electrochemical kinetic mechanisms were investigated through CV tests at low scan rates, galvanostatic intermittent titration technique (GITT) test, and *in-situ* electrochemical impedance spectroscopy (EIS) analysis. The CV curves of VS_4@Bi_2S_3-2 nanocomposite, VS_4 and Bi_2S_3 at scan rates of 0.1–1.0 mV·s^{-1} are shown in Fig. 4(a) and Fig. S21 in the ESM. One can see that the CV curves of the VS_4@Bi_2S_3 nanocomposite clearly exhibits characteristic peaks from VS_4 and Bi_2S_3, and maintains distinct peak shapes and high response currents even at progressively increasing scan rates, indicating its excellent rapid charge–discharge capability. To further investigate its kinetic advantages, the *b*-value was calculated by analyzing the relationship between peak current and scan rates (Fig. 4(b) and Fig. S22 in the ESM). The VS_4@Bi_2S_3-2 nanocomposite exhibits higher *b*-values than bare VS_4 and bare Bi_2S_3 materials in primary redox processes, indicating that its electrochemical process is more dominated by surface capacitive behavior with fast reaction kinetics [55], which is highly consistent with previous rate performance test results. Furthermore, this advantage was quantified by fitting the capacitive contribution (Fig. 4(c) and Figs. S23–S25 in the ESM). The pseudocapacitive contribution of VS_4@Bi_2S_3-2 at different scan rates consistently exceeds that of bare VS_4 and bare Bi_2S_3. Notably, the pseudocapacitive contribution of the VS_4@Bi_2S_3-2 electrode reached as high as 94.64% at a scan rate of 1 mV·s^{-1}. The high pseudocapacitive contribution indicates the presence of abundant rapidly accessible redox active sites within VS_4@Bi_2S_3-2. This is attributed to the moderate sulfur vacancy concentration in VS_4@Bi_2S_3-2 and the formation of a strong built-in electric field, which creates and exposes numerous highly active magnesium storage sites through interfacial bonding, as previously confirmed by EPR, XPS, and DFT predictions. Therefore, the high discharge capacity and outstanding rate performance achieved by the VS_4@Bi_2S_3 nanocomposite are mainly attributed to the rapid insertion/extraction of Mg^{2+} into the electrode material and its sufficient contact with the active sites.

Based on the GITT measurements shown in Fig. 4(d), the diffusion coefficients of Mg^{2+} ($D_{Mg^{2+}}$) in VS_4, Bi_2S_3, and VS_4@Bi_2S_3 were calculated (Fig. 4(e)). VS_4@Bi_2S_3-2 exhibited an order of magnitude higher $D_{Mg^{2+}}$ and charge/discharge time during cycling compared to the VS_4 and Bi_2S_3 materials, consistent with the lower diffusion energy barrier observed in DFT calculations for the nanocomposite structure. The significantly enhanced Mg^{2+} diffusion

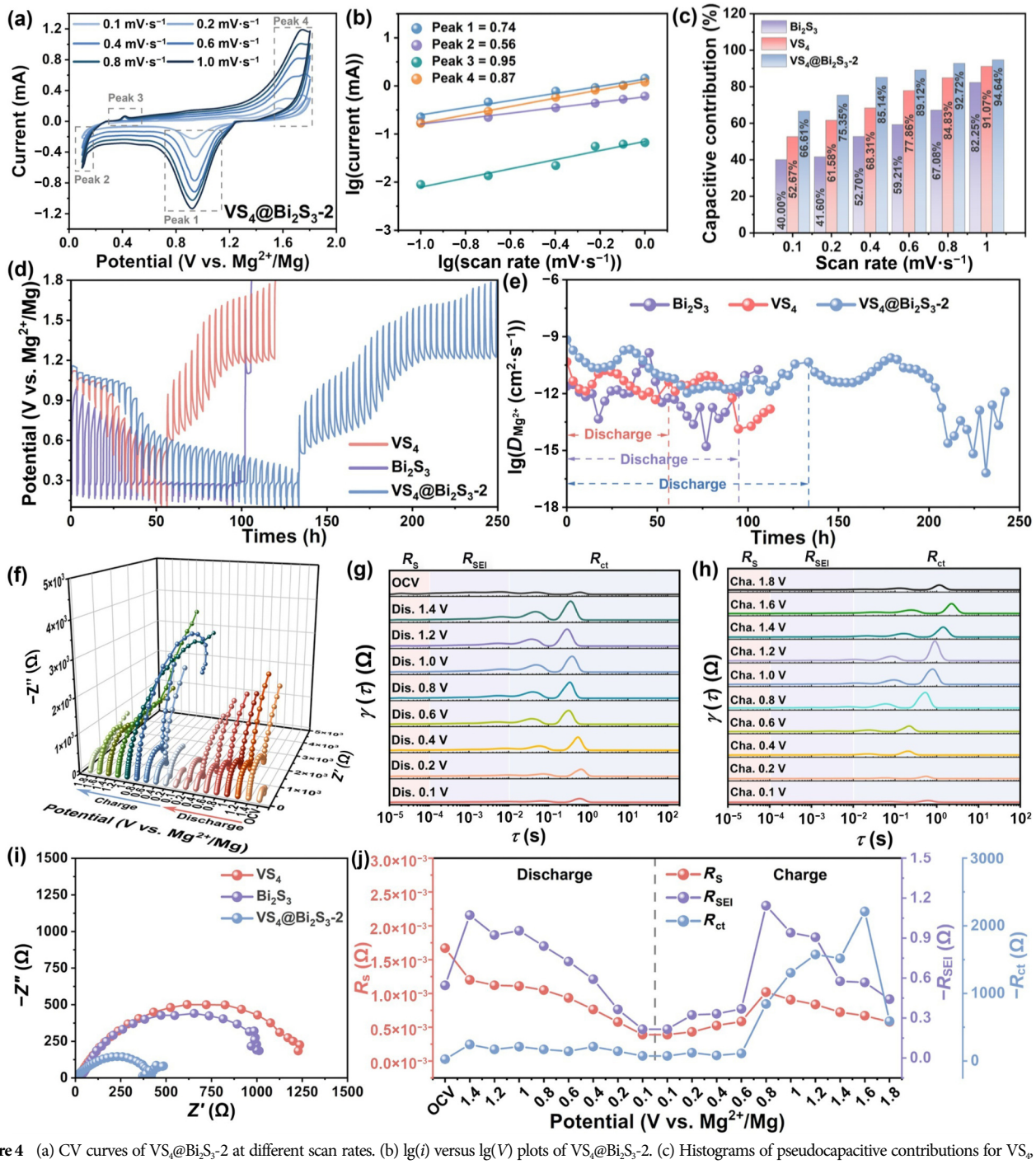

Figure 4 (a) CV curves of $VS_4@Bi_2S_3$-2 at different scan rates. (b) lg(*i*) versus lg(*V*) plots of $VS_4@Bi_2S_3$-2. (c) Histograms of pseudocapacitive contributions for VS_4, Bi_2S_3, and $VS_4@Bi_2S_3$-2 at different scan rates. (d) and (e) GITT plots and corresponding lg($D_{Mg^{2+}}$) values for VS_4, Bi_2S_3, and $VS_4@Bi_2S_3$-2. (f) *In-situ* Nyquist plot of $VS_4@Bi_2S_3$-2 during initial cycling. (g) and (h) DRT plots calculated from impedance measurements of $VS_4@Bi_2S_3$-2 during the first cycle. (i) Nyquist plots for VS_4, Bi_2S_3, and $VS_4@Bi_2S_3$-2. (j) Dependencies of R_S, R_{SEI}, and R_{ct} on discharge/charge potential.

coefficient directly confirms the positive regulation of ion transport kinetics through heterojunction interface engineering and defect engineering. This finding aligns with its exceptional rate performance, fully elucidating the origin of its high performance from the perspective of ion transport. To investigate the dynamic evolution process at the electrode interface, *in-situ* EIS measurements were performed on $VS_4@Bi_2S_3$-2 and analyzed the impedance of different processes using the distribution of relaxation times (DRT) (Figs. 4(f)–4(h) and Fig. S26 in the ESM). $VS_4@Bi_2S_3$-2 exhibits lower overall impedance at the initial state compared to VS_4 and Bi_2S_3 (Fig. 4(i) and Fig. S27 in the ESM), which is attributed to its superior initial conductivity provided by the heterointerface. By integrating DRT spectra, the evolution of the ohmic resistance (R_s), interfacial sheet resistance (R_{SEI}), and charge transfer resistance (R_{ct}) during charge–discharge cycles were quantitatively tracked (Fig. 4(j)). Throughout the discharge-charge process, the R_s of $VS_4@Bi_2S_3$-2 remained at a very low level, indicating stable contact within the battery structure [55]. Furthermore, it is observed that

the R_{SEI} of VS_4@Bi_2S_3-2 is lower at the initial discharge stage than at the undischarged state (Fig. 4(g)). Subsequently, R_s, R_{SEI}, and R_{ct} all gradually decrease during discharge process. When discharged to 0.1 V, R_{ct} (75.99 Ω) and R_{SEI} (0.216 Ω) reach their minimum values. These phenomena can be attributed to the initial formation of the SEI film during the early discharge stage. As discharge continues, a denser SEI film develops at the material interface, optimizing interfacial ion transport. Simultaneously, Mg^{2+} insertion elevates the state of charge of the material and improves its electronic conductivity, jointly reducing both R_{SEI} and R_{ct}. During charging, the R_{ct} of VS_4@Bi_2S_3-2 rises slowly, increases rapidly after 0.8 V, and then decreases at 1.8 V (Fig. 4(h)). This can be attributed to the gradual desorption of Mg^{2+} from Bi_2S_3 and VS_4. The reconstruction process of the VS_4 phase exhibits a higher kinetic energy barrier, increasing charge transfer resistance. At full charge, surface oxidation reactions on the electrode approach completion, stabilizing the interface and thereby lowering the charge transfer energy barrier [37]. These dynamic parameters collectively indicate that the VS_4@Bi_2S_3 heterojunction provides critical kinetic assurance for its outstanding electrochemical performance by establishing a highly active, ionically conductive, and stable interface during cycling.

To investigate the structural evolution of the VS_4@Bi_2S_3 heterostructure cathode under different charge/discharge states, *ex-situ* XRD measurements were performed during the first cycle within the 0.1–1.8 V. During discharge from open-circuit voltage to 0.1 V, the diffraction peak broaden, gradually weakens, and shifts to smaller angles (Fig. 5(a)), which directly confirms that Mg^{2+} successfully intercalates into the interstitial or interlayer spaces of the heterojunction, inducing overall lattice expansion. During charging from 0.1 to 1.8 V, characteristic diffraction peaks gradually intensified and exhibited peak position shift, confirming Mg^{2+} extraction and the excellent reversibility of the host crystal lattice structure. No distinct diffraction peaks for metallic V or Bi, nor for MgS, were observed in the overall XRD pattern (Fig. 5(b)), which suggests that the transformation reaction products in VS_4@Bi_2S_3-2 likely exist in a nanoscale or even amorphous state, rather than undergoing a conventional long-range ordered phase transition. In its previous charge–discharge curves, a voltage plateau first appeared due to Mg^{2+} intercalation into the VS_4 lattice (Eq. (1)), followed by a voltage plateau caused by Mg^{2+} intercalation into the Bi_2S_3 lattice (Eq. (2)). This indicates that during the initial discharge phase, Mg^{2+} preferentially inserts into the VS_4 lattice due to the combined effects of the built-in electric field at the heterointerface and lattice matching. During deep discharge, Mg^{2+} instead preferentially insert into Bi_2S_3, effectively suppressing excessive Mg^{2+} embedding in VS_4 and thereby preventing more irreversible conversion reactions (Eq. (3)). Furthermore, the discharge process

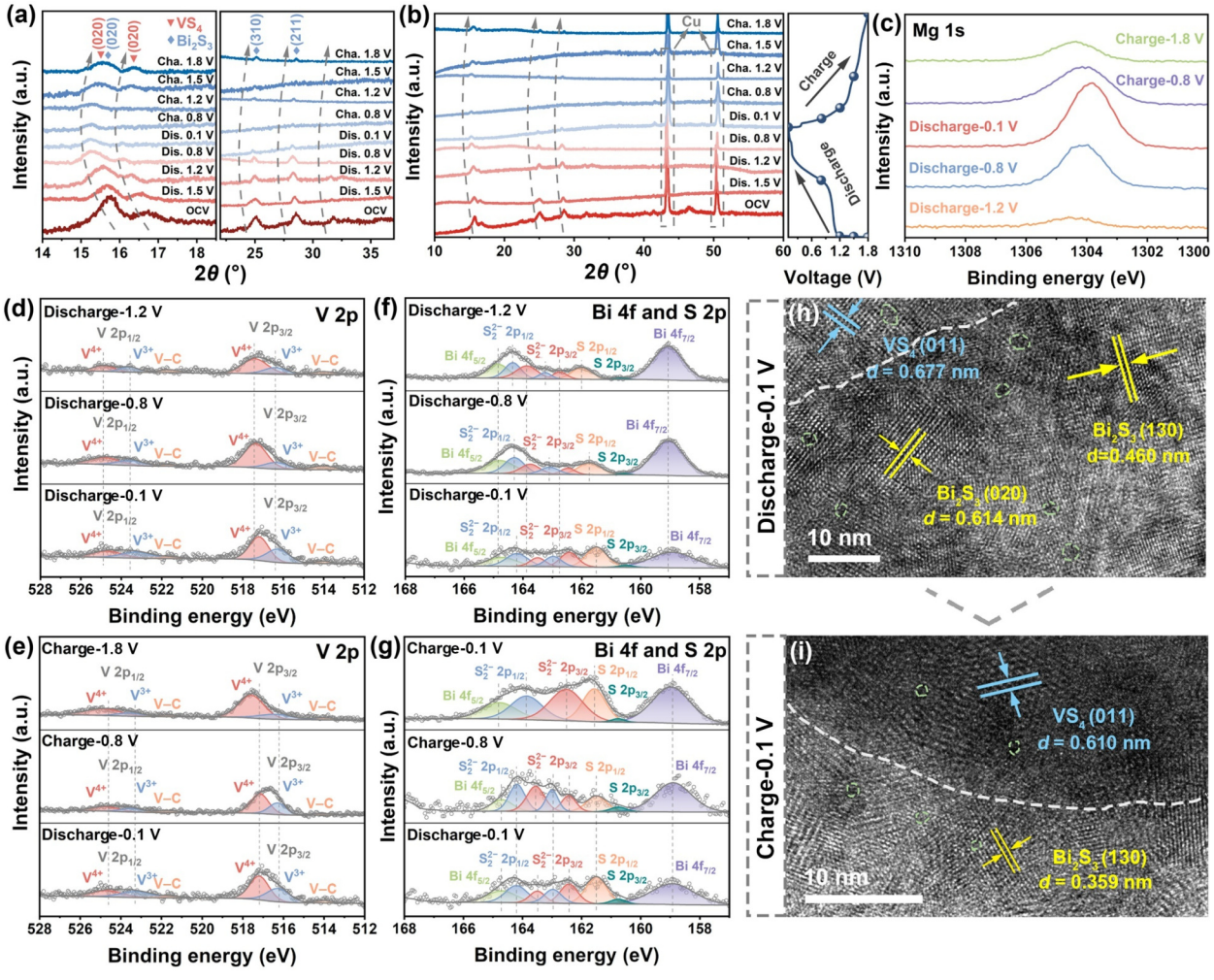

Figure 5 (a) and (b) *Ex-situ* XRD patterns of the VS_4@Bi_2S_3-2 heterostructure during the first cycle. *Ex-situ* XPS spectra of (c) Mg 1s, (d) and (e) V 2p, (f) and (g) Bi 4f and S 2p. (h) HRTEM image of VS_4@Bi_2S_3-2 during discharge to 0.1 V. (i) HRTEM image of VS_4@Bi_2S_3-2 during charge to 1.8 V.

between 0.2 and 0.1 V prevents excessive Mg^{2+} insertion into Bi_2S_3, thereby avoiding additional irreversible conversion reactions (Eq. (4)) [56, 57]. The synergy between intercalation and nanoconfined conversion significantly improves the cycling stability, as evidenced by the long-term cycling tests.

$$VS_4 + xMg^{2+} + 2xe^- \rightarrow Mg_xVS_4 \quad (1)$$

$$Bi_2S_3 + yMg^{2+} + 2ye^- \rightarrow Mg_yBi_2S_3 \quad (2)$$

$$Mg_xVS_4 + (4-x)Mg^{2+} + (8-2x)e^- \rightarrow V + 4MgS \quad (3)$$

$$Mg_yBi_2S_3 + (3-y)Mg^{2+} + (6-2y)e^- \rightarrow 2Bi + 3MgS \quad (4)$$

Furthermore, quantitative analysis of the Mg content via inductively coupled plasma-optical emission spectrometer (ICP-OES) during the initial charge–discharge cycle of the VS_4@Bi_2S_3-2 electrode (Fig. S28 in the ESM) further substantiates this process. Upon discharging to 0.1 V, the Mg content in the electrode corresponds to a calculated specific discharge capacity of 981.2 mAh·g^{-1}. This value aligns with the reversible capacity (1044.2 mAh·g^{-1}) estimated from the dQ/dV integration in Fig. S29 in the ESM, and is notably lower than the total discharge capacity (1407.7 mAh·g^{-1}). This result quantitatively distinguishes the capacity contributed by reversible Mg storage from that consumed by irreversible side reactions. After charging, approximately 67.6% of the Mg was extracted. This finding is consistent with the incomplete recovery of the VS_4 characteristic peak position observed in *ex-situ* XRD during cycling and the low Coulombic efficiency observed in the first cycle. Figures 5(c)–5(g) present *ex-situ* XPS results, dynamically revealing the electronic structure evolution of the VS_4@Bi_2S_3 heterostructure during charging and discharging process. The detailed XPS spectra show that the Mg 1s signal strengthens and shifts towards a lower binding energy during discharge (Fig. 5(c)), directly confirming the successful insertion of Mg^{2+}. Notably, during charging, the Mg 1s peak signal weakens and shifts to the left (indicating increased binding energy) before recovering. However, a Mg 1s signal persists even after charging completion, which indicates that a portion of Mg^{2+} are irreversibly trapped within the material structure, signifying an irreversible phase transition. This phenomenon reduces the ICE during GCD. In the high-resolution V 2p spectrum, the V^{3+}/V^{4+} peak shifts to the right during discharge, while the intensity of the V^{3+} peak increases (Fig. 5(d)). In turn, the V^{3+}/V^{4+} peak shifts to the left during charging, while the intensity of the V^{3+} peak weakens (Fig. 5(e)). This directly confirms the reversibility of the reaction: V ions are reduced during discharge ($V^{4+} \rightarrow V^{3+}$) and oxidized during charging ($V^{3+} \rightarrow V^{4+}$). This phenomenon perfectly aligns with computational results showing electron flow from Bi_2S_3 to VS_4 [58]. As an electron acceptor, the reduction of V is an inevitable consequence driven by the built-in electric field. Additionally, high-resolution XPS spectra of Bi 4f and S 2p reveal that the binding energy of Bi 4f shifts to the right and broadens during discharge (Fig. 5(f)), while both S_2^{2-} $2p_{3/2}$ and S_2^{2-} $2p_{1/2}$ split into two peaks. This indicates the transition of Bi^{3+} to Bi^0 and the dissociation of S-S dimers. During charging, the binding energy of Bi 4f shifts to the left and recovers, while both S_2^{2-} $2p_{3/2}$ and S_2^{2-} $2p_{1/2}$ return to single peaks (Fig. 5(g)). Although no independent Bi^0 signal was fitted from the Bi 4f spectrum in *ex-situ* XPS, we observed a systematic rightward shift in binding energy and broadening of the peak shape during discharge, which consistently indicates the reduction of Bi^{3+} during discharge [59, 60]. This further demonstrates the existence of a conversion reaction, the formation of nanoscale or amorphous products, and the excellent reversibility of both intercalation and conversion reactions during magnesium storage.

To visually investigate changes occurring during Mg^{2+} insertion/extraction from the material lattice during charging and discharging, *ex-situ* TEM measurement was conducted (Figs. 5(h) and 5(i)). Observation of the VS_4@Bi_2S_3-2 sample discharged to 0.1 V revealed significantly broadened lattice fringes compared to the pristine sample. Notably, numerous nanoscale regions of lattice disorder emerged within the originally ordered lattice stripes, indicating that conversion reactions occurred during discharge. These reactions generated ultrafine metallic V and Bi intermingled with the unreacted matrix, along with MgS [25]. After charging to 1.8 V, the lattice spacings of VS_4 and Bi_2S_3 decreased, confirming the reversible intercalation/deintercalation of Mg^{2+}. However, partially irreversible nanocrystalline domains remained observable in TEM images. This finding correlates with residual Mg signals in XPS and sub-100% ICE in GCD, collectively demonstrating the presence of minor irreversible conversion reaction products. Furthermore, *ex-situ* TEM combined with EDS line scanning was performed to reveal the distribution of Mg within the VS_4 and Bi_2S_3 phases (Fig. S30 in the ESM). Upon discharging to 0.1 V, Mg was not uniformly distributed, and it was found to preferentially accumulate at the heterointerfaces and within the spherical VS_4 regions. A dispersed Mg signal was also detected in the Bi_2S_3 nanorod regions, which further confirms the successful construction of the heterointerface. Notably, a residual Mg signal was still detectable after charging to 1.8 V, indicating that Mg^{2+} was not fully reversibly extracted during the initial cycle. This observation aligns with and is corroborated by the results obtained from *ex-situ* XPS and ICP-OES measurements. The SEM images after the cycle further elucidate the macrostructural stability mechanism of the heterostructure (Fig. S31 in the ESM). After 50 cycles at 0.05 A·g^{-1}, the epitaxial Bi_2S_3 nanorods collapsed and reorganized, uniformly forming a Bi_2S_3 particle coating layer on the spherical VS_4 surface. This restructuring not only preserved the system integrity, but also created tighter interfacial contact. After 2000 cycles at 1 A·g^{-1}, although the structure collapsed inward, the VS_4 still retained a layer of Bi_2S_3 particles. XPS analysis of the VS_4@Bi_2S_3-2 electrode after 2000 cycles (Fig. S32 in the ESM) reveals that the V 2p, Bi 4f, and S 2p spectra are highly similar to those of the pristine, uncycled state. This indicates that the bulk chemical structure of the active material is largely preserved after prolonged cycling, retaining its fundamental ability to undergo reversible valence state changes. From a chemical bonding perspective, this explains the origin of its high capacity retention. The XRD pattern of the long-term cycled electrode (Fig. S33 in the ESM) shows that the characteristic diffraction peak intensities for both VS_4 and Bi_2S_3 are significantly weakened. Furthermore, relatively weak diffraction peaks corresponding to MgS and Bi_2Mg_3 emerge. This can be attributed to a surface structural reconstruction and a confined nanoscale conversion process undergone by VS_4@Bi_2S_3-2, where the restructuring of the Bi_2S_3 nanorod architecture leads to a more thorough encapsulation of the VS_4 component. This fully demonstrates the role of the uniform Bi_2S_3 layer in relieving volumetric stress on the VS_4 during cycling, thereby significantly enhancing the overall structural integrity of the electrode. This is one of the key reasons for its outstanding long-cycle stability.

3 Conclusions

This study successfully demonstrates an effective strategy for precisely designing high-performance RMBs cathode materials through synergistic coupling of defect engineering and heterojunction interface engineering. By precisely controlling the ratio of vanadium-bismuth precursors, the VS_4@Bi_2S_3 heterostructure with moderate sulfur vacancy concentration and interface coupling was synthesized via rapid microwave-assisted solvothermal method. A moderate amount of sulfur vacancies provides sufficient active sites while avoiding structural degradation caused by high defect concentrations. Meanwhile, the uniform heterointerface simultaneously promotes charge transport and serves as a mechanical framework that buffers volume changes. Theoretical calculations confirm that the heterojunction forms Type-II band alignment, where the generated built-in electric field synergistically interacts with interfacial orbital hybridization. This modification significantly improves the intrinsic electronic conductivity of the material and concurrently lowers both the adsorption energy and diffusion energy barrier for Mg^{2+}. Electrochemical testing, coupled with multiple *in-situ*/*ex-situ* characterizations, collectively revealed a synergistic mechanism of intercalation-nanoconfinement transformation. VS_4 preferentially undergoes reversible intercalation reactions, followed by a highly reversible transformation reaction confined to the nanoscale, guided by the heterojunction. This simultaneously achieves high capacity and long cycle life. Furthermore, *in-situ* EIS and post-cycling micromorphology analysis revealed that the heterojunction interface dynamically reconfigured into a stable protective layer during long-term cycling, effectively alleviating stress and serving as the key to its outstanding structural stability. Ultimately, the optimized VS_4@Bi_2S_3 electrode exhibited a high reversible specific capacity of 389.42 mAh·g^{-1} after 50 cycles at 0.05 A·g^{-1}, high rate performance, and maintaining excellent stability even after 2000 cycles at a high current density of 1 A·g^{-1}. This work provides a new method for rationally designing stable electrode structures for multivalent ion storage systems through multi-engineering synergistic strategies. Specifically, it embodies a path for rapidly preparing heterostructure materials, and thereby successfully developed high-performance electrode materials.

Electronic Supplementary Material: Supplementary material (material characterization, fabrication of RMBs devices and electrochemical measurements, theoretical calculation methods, Figs. S1–S33, and Table S1) is available in the online version of this article at https://doi.org/10.26599/NR.2026.94908461.

Acknowledgements

This work was supported by the National Natural Science Foundation of China (Nos. 22269020 and 42167068), Natural Science Foundation of Gansu Province (Nos. 25JRRA004 and 22JR5RA813), and Hubei Provincial Natural Science Foundation of China (Nos. 2024DJC032 and 2025AFB889). I. S. wishes to extend his sincere gratitude to the Deanship of Scientific Research at the Islamic University of Madinah (KSA) for the support provided through the Post-Publishing Program.

Data availability

All data needed to support the conclusions in the paper are presented in the manuscript and the Electronic Supplementary Material. Additional data related to this paper may be requested from the corresponding author upon request.

Declaration of competing interest

All the contributing authors report no conflict of interests in this work.

Author contribution statement

H. P.: Conceptualization. J. T. Z. and S. B. X.: Methodology, investigation. S. B. X. and P. Y. X.: Validation. J. T. Z. and X. X.: Formal analysis. H. P. and J. T. Z.: Data curation. J. T. Z.: Software. J. T. Z. and X. X.: Visualization. H. P., L. Z., I. S., and G. F. M.: Funding acquisition. H. P.: Project administration. G. F. M. and Y. X. X.: Supervision. H. P., L. Z., I. S., G. F. M., and Y. X. X. Resources. J. T. Z.: Writing – original draft. H. P. and Y. X. X.: Writing – review & editing. All authors reviewed the data and analysis, provided input on the manuscript, and approved the submission.

Use of AI statement

None.

References

[1] Wang, D.; Zhang, Z. Y.; Hao, Y.; Jia, H. X.; Shen, X.; Qu, B. H.; Huang, G. S.; Zhou, X. Y.; Wang, J. F.; Xu, C. H. et al. Challenges and progress in rechargeable magnesium-ion batteries: Materials, interfaces, and devices. *Adv. Funct. Mater.* **2024**, *34*, 2410406.

[2] Abdalla, A. M.; Abdullah, M. F.; Dawood, M. K.; Wei, B.; Subramanian, Y.; Azad, A. T.; Nourin, S.; Afroze, S.; Taweekun, J.; Azad, A. K. Innovative lithium-ion battery recycling: Sustainable process for recovery of critical materials from lithium-ion batteries. *J. Energy Storage* **2023**, *67*, 107551.

[3] Viswanathan, V.; Epstein, A. H.; Chiang, Y. M.; Takeuchi, E.; Bradley, M.; Langford, J.; Winter, M. The challenges and opportunities of battery-powered flight. *Nature* **2022**, *601*, 519–525.

[4] Pan, Q. G.; Zheng, Y. P.; Tong, Z. P.; Shi, L.; Tang, Y. B. Novel lamellar tetrapotassium pyromellitic organic for robust high-capacity potassium storage. *Angew. Chem., Int. Ed.* **2021**, *60*, 11835–11840.

[5] Yu, Q.; Shi, X. J.; Zhang, T. Q.; Zhao, Y.; Jin, J.; Wang, R.; Gong, Y. S.; Wang, H. W. Hollow carbon fibers with balanced graphitization and defects for extremely fast-charging potassium storage. *Nano Res.* **2026**, *19*, 94908253.

[6] Lu, G. J.; Li, M. H.; Chen, P.; Zheng, W. K.; Yang, Z. G.; Wang, R. H.; Xu, C. H. Built-in superionic conductive phases enabling dendrite-free, long lifespan and high specific capacity composite lithium for stable solid-state lithium batteries. *Energy Environ. Sci.* **2023**, *16*, 1049–1061.

[7] Song, B.; Cheng, Y. B.; Zhao, G. G.; Jia, K. S.; Shi, Q. M.; Li, X. D.; Wang, Z. G.; Zhou, Y. L.; Zou, G. Q.; Ji, X. B. Sodium ion batteries: From basic research to industrialization. *Adv. Funct. Mater.* **2025**, *35*, e10872.

[8] Niu, J. Z.; Zhang, Z. H.; Aurbach, D. Alloy anode materials for rechargeable Mg ion batteries. *Adv. Energy Mater.* **2020**, *10*, 2000697.

[9] Li, Z. Y.; Häcker, J.; Fichtner, M.; Zhao-Karger, Z. Cathode materials and chemistries for magnesium batteries: Challenges and opportunities. *Adv. Energy Mater.* **2023**, *13*, 2300682.

[10] Shi, H. C.; Wang, G. X.; Wang, Z. C.; Yang, L.; Zhang, S.; Dong, S. M.; Qu, B. H.; Du, A. B.; Li, Z. Y.; Zhou, X. Y. et al. Understanding the cathode-electrolyte interfacial chemistry in rechargeable magnesium batteries. *Adv. Sci.* **2024**, *11*, 2401536.

[11] Tian, Y. S.; Zeng, G. B.; Rutt, A.; Shi, T.; Kim, H.; Wang, J. Y.; Koettgen, J.; Sun, Y. Z.; Ouyang, B.; Chen, T. N. et al. Promises and challenges of next-generation "beyond Li-ion" batteries for electric vehicles and grid decarbonization. *Chem. Rev.* **2021**, *121*, 1623–1669.

[12] Mao, M. L.; Gao, T.; Hou, S.; Wang, C. S. A critical review of cathodes for rechargeable Mg batteries. *Chem. Soc. Rev.* **2018**, *47*, 8804–8841.

[13] Lei, X.; Liang, X.; Yang, R.; Zhang, F.; Wang, C. C.; Lee, C. S.; Tang, Y. B. Rational design strategy of novel energy storage systems: Toward high-performance rechargeable magnesium batteries. *Small* **2022**, *18*, 2200418.

[14] Zhang, D.; Duan, S. Z.; Liu, X. S.; Yang, Y.; Zhang, Y.; Ren, W.; Zhang, S. X.; Cheng, M. X.; Yang, W. J.; Wang, J. L. et al. Deeping insight of $Mg(CF_3SO_3)_2$ and comprehensive modified electrolyte with ionic liquid enabling high-performance magnesium batteries. *Nano Energy* **2023**, *109*, 108257.

[15] Zhang, J. L.; Liu, J.; Wang, M.; Zhang, Z. H.; Zhou, Z. F.; Chen, X.; Du, A. B.; Dong, S. M.; Li, Z. J.; Li, G. C. et al. The origin of anode-electrolyte interfacial passivation in rechargeable Mg-metal batteries. *Energy Environ. Sci.* **2023**, *16*, 1111–1124.

[16] Cao, H.; Zhu, Y. Q.; Jiang, T.; Leng, Z. Y.; Yu, H. Y.; Ma, X. L.; Cao, C. B.; Zou, M. S. Fundamental understanding and material challenges in rechargeable magnesium-sulfur battery: Current advances and perspective. *Small* **2025**, *21*, e07241.

[17] Huang, M.; Wang, X. P.; Wang, J. J.; Meng, J. S.; Liu, X.; He, Q.; Geng, L. S.; An, Q. Y.; Yang, J. L.; Mai, L. Proton/Mg^{2+} Co-insertion chemistry in aqueous Mg-ion batteries: From the interface to the inner. *Angew. Chem., Int. Ed.* **2023**, *62*, e202308961.

[18] Xu, R. J.; Gao, X.; Chen, Y.; Peng, C. X.; Zhang, Z. Y.; Wang, C.; Sun, H. C.; Chen, X. D.; Cui, L. F. Research advances of the electrolytes for rechargeable magnesium ion batteries. *Mater. Today Phys.* **2023**, *36*, 101186.

[19] Regulacio, M. D.; Nguyen, D. T.; Horia, R.; Seh, Z. W. Designing nanostructured metal chalcogenides as cathode materials for rechargeable magnesium batteries. *Small* **2021**, *17*, 2007683.

[20] Miao, W. X.; Peng, H.; Cui, S. Z.; Zeng, J. T.; Ma, G. F.; Zhu, L.; Lei, Z. Q.; Xu, Y. X. Fine nanostructure design of metal chalcogenide conversion-based cathode materials for rechargeable magnesium batteries. *iScience* **2024**, *27*, 109811.

[21] Chinnadurai, D.; Lieu, W. Y.; Kumar, S.; Yang, G. L.; Li, Y. J.; Seh, Z. W. A passivation-free solid electrolyte interface regulated by magnesium bromide additive for highly reversible magnesium batteries. *Nano Lett.* **2023**, *23*, 1564–1572.

[22] Das, A.; Balakrishnan, N. T. M.; Sreeram, P.; Fatima, M. J. J.; Joyner, J. D.; Thakur, V. K.; Pullanchiyodan, A.; Ahn, J. H.; Raghavan, P. Prospects for magnesium ion batteries: A compreshensive materials review. *Coordin. Chem. Rev.* **2024**, *502*, 215593.

[23] Jiang, R.; Jin, M. W.; Du, C. L.; Song, T. L.; Ma, X. L.; Zhu, Y. Q.; Cao, C. B.; Zou, M. S. Rich Se vacancies $Mo_xV_{1-x}Se_2$ nanosheets with synergistic optimization of electronic and lattice structures for accelerating sulfur redox kinetics in Mg–S batteries. *Adv. Energy Mater*. **2025**, e05028.

[24] Chen, F. Y.; Huang, K. F.; Li, H. Y.; Zhong, Q.; Yue, J. L.; Diao, J.; Wang, Z. T.; Huang, G. S.; Jiang, B.; Pan, F. S. Interlayer cationic defect engineering in lamellar vanadate cathodes enables ultralong-lifespan magnesium-ion batteries. *ACS Energy Lett.* **2025**, *10*, 2052–2060.

[25] Jiang, R.; Liu, B. L.; Du, C. L.; Jin, M. W.; Liu, X.; Ma, X. L.; Zhu, Y. Q.; Zou, M. S.; Cao, C. B. Microwave-induced defect-rich vanadium sulfide cathodes for highly reversible electrochemical magnesium storage. *Chem. Eng. J.* **2024**, *488*, 150487.

[26] Zhang, X. Y.; Li, W. X.; Sun, M. H.; Wu, M.; Liu, F. F.; Zhou, D. Rational design of MXene@VS_4 heterostructures via interfacial coupling for advanced magnesium-ion batteries. *J. Energy Chem.* **2025**, *109*, 566–575.

[27] Chen, W. W.; Sun, Q. H.; Li, J. C.; Gong, Z. W.; Xie, W. J.; Ouyang, Z. Y.; Zheng, B.; Zhao, J.; Xiao, Y. H.; Lei, S. J. et al. Modulation of surface/interface states in Bi_2S_3/VS_4 heterostructure with CN layer for high-performance sodium-ion batteries: Enhanced built-in electric field and polysulfide capture. *Small* **2025**, *21*, 2500359.

[28] Chen, J. K.; Wang, G. F.; Sun, B.; Zhang, Y.; Li, M. Y.; Wang, L.; Li, G. C.; Meng, A. L.; Ding, S. Q.; Li, Z. J. Defect engineering for achieving multi-electrons storage in VS_4 to enhance magnesium storage performance. *Nano Res.* **2024**, *18*, 94907393.

[29] Li, W. T.; Zhang, Q. F.; Pei, Q.; Yang, Y.; Zhao, J. X.; Xie, S. H.; Huang, J. Y. Bi_2S_3 confined by covalent organic frameworks enables high-rate high-capacity potassium storage. *Adv. Funct. Mater.* **2024**, *34*, 2404197.

[30] Li, Y. N.; Li, T. Y.; Deng, Y. R.; Tang, W. H.; Wu, H.; Feng, M.; Yan, P.; Liu, R. P. Tuning the D-band center of Bi_2S_3–MoS_2 heterostructure towards superior lithium-sulfur batteries. *Small* **2024**, *20*, 2401921.

[31] Liu, X. N.; Liu, X. B.; Li, C. X.; Yang, B.; Wang, L. Defect engineering of electrocatalysts for metal-based battery. *Chin. J. Catal.* **2023**, *45*, 27–87.

[32] Zhang, H.; Zhao, Z. B.; Hou, Y. N.; Tang, Y. C.; Liang, J. J.; Liu, X. G.; Zhang, Z. C.; Wang, X. Z.; Qiu, J. S. Highly stable lithium-sulfur batteries based on p-n heterojunctions embedded on hollow sheath carbon propelling polysulfides conversion. *J. Mater. Chem. A* **2019**, *7*, 9230–9240.

[33] Song, X. X.; Wang, J. J.; Jiang, Q. T.; Li, M.; Duan, R. X.; Li, J.; Li, W. B.; Xiao, W.; Zhang, G. N.; Xie, C. et al. Tuning D-band center of vanadium in constructing lattice-matched coherent heterostructure for enhanced sodium storage. *Adv. Funct. Mater.* **2025**, *35*, 2502181.

[34] Yu, J. Z.; Tang, Q. K.; Liu, Y. N.; Zhu, Y. F.; Zhang, J. G.; Wang, J.; Li, L. Q. Construction of TiO_2/$TiOF_2$ heterojunction as a cathode material for high-performance Mg^{2+}/Li^+ hybrid-ion batteries. *J. Colloid Interface Sci.* **2023**, *646*, 587–596.

[35] Ding, S. Q.; Dai, X.; Li, Z. J.; Wang, C. S.; Meng, A. L.; Wang, L.; Li, G. C.; Huang, J. F.; Li, S. X. PVP-induced synergistic engineering of interlayer, self-doping, active surface and vacancies in VS_4 for enhancing magnesium ions storage and durability. *Energy Storage Mater.* **2022**, *47*, 211–222.

[36] Bo, S. F.; Luo, J. M.; Lee, J. W.; Kim, K. H. Interfacial electron regulation of $Fe_9Ni_9S_{16}$/FeS heterostructure confined in N-doped carbon nanotube with enhanced reaction kinetics for efficient Na/Li-Ion storage. *J. Energy Chem.* **2025**, *107*, 459–471.

[37] Zheng, H.; Ma, D. K.; Pei, M. J.; Lin, C. K.; Liu, Y.; Deng, S. Q.; Qiu, R. X.; Luo, Y. Y.; Yan, W.; Zhang, J. J. Heterojunction vacancies-promoted high sodium storage capacity and fast reaction kinetics of the anodes for ultra-high performance sodium-ion batteries. *Adv. Funct. Mater.* **2025**, *35*, 2411651.

[38] Li, E. Z.; Wang, M. S.; Xu, W.; Höche, D.; Feng, Y. L.; Chen, J. C.; Yu, B.; Guo, B. S.; Ma, Z. Y.; Huang, Y. et al. VS_2/Bi_2S_3 spring-type heterointerfaces hollow microspheres with spatial confinement and vacancy defects for fast-charging and ampere-hour scale pouch sodium-ion hybrid capacitors. *Adv. Energy Mater.* **2025**, *15*, 2405674.

[39] Wang, X. C.; Zhang, X.; Chen, Y.; Dong, J. Q.; Zhao, J. Optimizing electron spin-polarized states of $MoSe_2$/Cr_2Se_3 heterojunction-embedded carbon nanospheres for superior sodium/potassium-ion battery performances. *Small* **2024**, *20*, 2312130.

[40] Kong, L. Q.; Qiao, J. Y.; Li, W.; Xia, L. H.; Yan, B. Z.; Zhang, S.; Ruan, Q. S.; Sun, Z. M. Regulating charge transfer in a heterojunction photoanode for efficient photo-charging of Zn-air/sulfion hybrid batteries. *Adv. Funct. Mater.* **2025**, *35*, 2417892.

[41] Ding, S. Q.; Dai, X.; Li, Z. J.; Meng, A. L.; Wang, L.; Li, G. C.; Li, S. X. Strategy of cation/anion co-doping for potential elevating of VS_4 cathode for magnesium ion batteries. *Chem. Eng. J.* **2022**, *439*, 135778.

[42] Yang, M.; Lin, Y. R.; Chen, P. W.; Lai, M. N.; Zhu, J. H.; Li, G. M.; Chen, M. F.; Wang, Y. Y.; Chuai, M.; Chen, J. Z. et al. Unlocking ultrafast-kinetics asymmetric heterojunction with multi-anionic redox

chemistry enables high energy/power density and low-temperature zinc-ion batteries. *Angew. Chem., Int. Ed.* **2025**, *64*, e202510907.

[43] Zhao, Y. W.; Ma, L. T.; Zhu, Y. B.; Qin, P.; Li, H. F.; Mo, F. N.; Wang, D. H.; Liang, G. J.; Yang, Q.; Liu, W. S. et al. Inhibiting grain pulverization and sulfur dissolution of bismuth sulfide by ionic liquid enhanced poly(3, 4-ethylenedioxythiophene): Poly(styrenesulfonate) for high-performance zinc-ion batteries. *ACS Nano* **2019**, *13*, 7270–7280.

[44] He, X. Q.; Cheng, R. Q.; Sun, X. Y.; Sun, F. Z.; Fu, Y.; Li, Y. T.; Li, P.; Li, Z.; Xu, H.; Laine, R. M. et al. Organic heterophase composites induced sulfur vacancies and internal electric field enhancement for advanced magnesium storage of copper sulfide cathodes. *Adv. Funct. Mater.* **2025**, *35*, 2413893.

[45] Wang, J. B.; Tan, X. Y.; Ng, M. F.; Wu, G.; Yang, G. L.; Ghosh, T.; Lim, C. Y. J.; Busayaporn, W.; Limphirat, W.; Kaewsuwan, D. et al. Hybrid redox chemistry in defective titanium polyanion nanobelt cathodes for advanced magnesium-ion batteries. *Adv. Funct. Mater.* **2026**, *36*, e12519.

[46] Liu, Y. H.; Qu, B. H.; Tang, Z. M.; Yue, J. L.; Tong, L.; Wan, J. J.; Li, S. Y.; Huang, G. S.; Li, Q.; Paillard, E. et al. Fast phase transformation enabled by Cu single atom stabilized 1T-rich MoS_2 for efficient magnesium ion storage. *Adv. Funct. Mater.* **2025**, *35*, 2502580.

[47] Xia, Y. P.; Chen, C. X.; Ran, L.; Zhang, H. A.; Cui, S.; Xiao, P. F.; Xu, F.; Zhang, D. H.; Li, T. Preferentially *in-situ* generated copper nanograins boosting fast kinetic conversion magnesium storage of bimetallic copper-cobalt sulfide cathode. *Chem. Eng. J.* **2024**, *488*, 151133.

[48] Guo, W. Q.; Hanaor, D. A. H.; Kober, D.; Wang, J.; Bekheet, M. F.; Gurlo, A. Rechargeable magnesium ion batteries based on nanostructured tungsten disulfide cathodes. *Batteries* **2022**, *8*, 116.

[49] Li, J. B.; Xu, Y. F.; He, Y. N.; Zhang, Z. Z.; Zhu, C. N.; Zhou, X. S. Core-shell-structured carbon nanotube@VS_4 nanonecklaces as a high-performance cathode material for magnesium-ion batteries. *J. Phys. Chem. Lett.* **2022**, *13*, 5726–5733.

[50] Ye, Z. S.; Li, P.; Wei, W. T.; Huang, C.; Mi, L. W.; Zhang, J. L.; Zhang, J. J. *In situ* anchoring anion-rich and multi-cavity NiS_2 nanoparticles on NCNTs for advanced magnesium-ion batteries. *Adv. Sci.* **2022**, *9*, 2200067.

[51] Zeng, J. T.; Miao, W. X.; Wang, D. Y.; Yan, C. H.; Zhang, Z.; Peng, H.; Ma, G. F.; Lei, Z. Q. Heterointerface engineering-induced V–C bonds and built-in electric field boosts Mg^{2+} storage and diffusion kinetics. *ACS Sustainable Chem. Eng.* **2025**, *13*, 14600–14611.

[52] Liu, J. Y.; Liu, J. M.; Zhou, T.; Huang, X. F.; Zhu, Y. J.; Xu, H. J.; Han, T. L. High-performance magnesium/lithium hybrid-ion battery using NiS_2 nanosheet-coated Cu_2S cubes as a cathode material. *ACS Appl. Mater. Interfaces* **2025**, *17*, 38041–38049.

[53] Liu, X.; Zhu, Y. Q.; Du, C. L.; Tian, J. C.; Yang, L. F.; Yao, X. Y.; Wang, Z. T.; Ma, X. L.; Hou, J. H.; Cao, C. B. Cationic Co-doping in copper sulfide nanosheet cathodes for efficient magnesium storage. *Chem. Eng. J.* **2023**, *463*, 142433.

[54] Jing, P. C.; Stevenson, S.; Lu, H. M.; Ren, P.; Abrahams, I.; Gregory, D. H. Pillared vanadium molybdenum disulfide nanosheets: Toward high-performance cathodes for magnesium-ion batteries. *ACS Appl. Mater. Interfaces* **2023**, *15*, 51036–51049.

[55] Peng, H.; Miao, W. X.; Zeng, J. T.; Wang, Z. H.; Yan, C. H.; Ma, G. F.; Lei, Z. Q. Electronic modulation and built-in electric field strategies in heterostructures together induce 1T-rich MoS_2 conversion for advanced sodium storage. *Adv. Sci.* **2025**, *12*, 2417288.

[56] Jankowski, P.; Lastra, J. M. G. Towards the understanding of (dis)charging mechanism of VS_4 cathode for magnesium batteries. *J. Energy Storage* **2023**, *62*, 106895.

[57] Du, Y. B.; Wang, Z. T.; Tian, M.; Ma, H. P.; Li, D. S.; Zhang, W. M.; Yang, H. Y.; Chen, S. Interfacial coupling toward bismuth sulfide/MXene heterostructures empowering reversible magnesium storage. *ACS Appl. Mater. Interfaces* **2024**, *16*, 44636–44644.

[58] Wang, Y. R.; Liu, Z. T.; Wang, C. X.; Yi, X.; Chen, R. P.; Ma, L. B.; Hu, Y.; Zhu, G. Y.; Chen, T.; Tie, Z. et al. Highly branched VS_4 nanodendrites with 1D atomic-chain structure as a promising cathode material for long-cycling magnesium batteries. *Adv. Mater.* **2018**, *30*, 1802563.

[59] Tao, D. G.; Li, T.; Tang, Y. D.; Gui, H. D.; Cao, Y. L.; Xu, F. Mo_3S_{13} cluster-based cathodes for rechargeable magnesium batteries: Reversible magnesium association/dissociation at the bridging disulfur along with sulfur-sulfur bond break/formation. *ACS Nano* **2024**, *18*, 5590–5598.

[60] Xie, M. G.; Li, C. G.; Zhang, S. Q.; Zhang, Z.; Li, Y. X.; Chen, X. B.; Shi, Z.; Feng, S. H. Topological insulator Bi_2Se_3-assisted heterostructure for ultrafast charging sodium-ion batteries. *Small* **2023**, *19*, 2301436.